Nano Research

ISSN 1998-0124 CN 11-5974/O4
https://doi.org/10.1007/s12274-021-3886-x

Research Article

Rare-earth single atom based luminescent composite nanomaterials: Tunable full-color single phosphor and applications in WLEDs

Shan Bao[1], Haiyue Yu[1], Guoyang Gao[1], Hongyang Zhu[2], Dingsheng Wang[3], Peifen Zhu[4] (✉), and Guofeng Wang[1] (✉)

[1] *Key Laboratory of Functional Inorganic Material Chemistry, Ministry of Education, School of Chemistry and Materials Science, Heilongjiang University, Harbin 150080, China*
[2] *School of Physics and Electronic Engineering, Linyi University, Linyi 276005, China*
[3] *Department of Chemistry, Tsinghua University, Beijing 100084, China*
[4] *Department of Physics and Engineering Physics, The University of Tulsa, Tulsa, OK 74104, USA*

Received: 15 August 2021 / **Revised:** 13 September 2021 / **Accepted:** 14 September 2021

ABSTRACT

High-quality single-component white phosphors are instrumental in realizing high-efficiency devices. Rare earth fluorides and carbon quantum dots have great potential in the white light-emitting diode (WLED) field due to their unique advantages. Here, Rare-earth single atom based $NaGdF_4$:Tb^{3+}/Eu^{3+}@C:N/Eu^{3+} single phosphor with tunable full-color luminescence was reported. The results of density functional theory (DFT) calculation and experimental characterization show that C atoms cannot be replaced by Eu^{3+}, but C atoms are more favorable for anchoring Eu^{3+} single atoms. The DFT was employed to optimize the structures of the C:N/Eu^{3+} and $NaGdF_4$:Tb^{3+}/Eu^{3+}, and calculate the work function, optical properties, and charge density difference. The obtained tunable full-color single phosphor can emit stable light from blue to red or even white. The constructed WLED devices also have stable and excellent color performance, that is, a color rendering index of up to 95 and a lower color temperature, and it has broad application possibilities in WLEDs.

KEYWORDS

single atoms, luminescence, single phosphor, white light-emitting diodes

1 Introduction

White light-emitting diodes (WLEDs) have become the most promising lighting technology and almost dominated the current lighting field due to their high energy efficiency, long service life, fast response speed, and high reliability [1–5]. Meanwhile, WLEDs are also the potential competitors in the manufacture of multi-color displays, low-cost backlighting of liquid crystal displays, and the next generation of light sources in our daily lives. Currently, the most widely used WLEDs are usually made of InGaN blue chips and YAG:Ce^{3+} yellow phosphors. However, the disadvantage of this type of WLEDs is the lack of red light in the emission spectrum, which results in high correlated color temperature (CCT), low color rendering index (CRI), and blue light hazards. The above shortcomings and hazards limit the practical application of WLED devices based on blue chips [6, 7]. In recent years, to reduce the impact of blue light chips and obtain higher-performance WLEDs, researchers have turned their attention to tricolor emitting phosphor which is excited by short-wavelength near-ultraviolet light (NUV) chips [8–13].

In general, high-quality white light emission can be achieved by mixing and tuning the relative intensity of the blue (B), green (G), and red (R) emission [14–17]. The white light achieved by R/G/B phosphors has a small color difference and high color purity. Although this approach can achieve coordinated white light, it has disadvantages such as strong reabsorption, mismatched aging rates, and uneven thermal quenching. Fortunately, in terms of solving the above problems, the method of using a single component to emit white light is more advanced and is now receiving more and more attention. In order to overcome these shortcomings, WLEDs could be fabricated by coating white light single-phase phosphors on NUV-LED chips because it has advantages including high CRI, high color stability, reproducibility, and reduced retinal damage [18–20]. Therefore, the design and development of single-phase solid-state phosphors are extremely important for achieving high-efficiency WLEDs and speeding up their applications.

Currently, various materials that can be used for WLEDs have been explored, including nitrides, oxides, metal–organic frameworks (MOFs), and perovskites [21–24]. Especially, carbon quantum dots (CQDs) generally have the characteristics of high luminosity, good stability, low toxicity, low preparation costs, and easy functionalization [25, 26]. It has adjustable emission with a narrow full-width at half-maximum (FWHM), which avoids the photobleaching phenomenon and becomes an attractive blue emission source for LEDs.

Rare earth (RE) luminescent materials have been implemented

Address correspondence to Guofeng Wang, 2010070@hlju.edu.cn; Peifen Zhu, peifen-zhu@utulsa.edu

in modern optoelectronic devices due to the unique electronic structure, abundant energy levels, and characteristic emission of RE ions. RE luminescent materials have the advantages of wide emission spectrum range, narrow linewidth emission, adjustable excitation range, and stable physical and chemical properties. Taking RE ions as the luminescence center is still the main strategy for developing WLED phosphors with excellent color quality and luminescence performance [27, 28]. $NaGdF_4$ is a common ideal host material, which not only can realize the Ln^{3+} dopant to generate down-shift emission, but also has high photochemical stability, low phonon energy, and high transparency in the ultraviolet–visible–near infrared (UV–vis–NIR) region [29, 30]. In particular, it can also mediate energy transfer among Ln^{3+} ions. Therefore, $NaGdF_4$ can be doped with Ln^{3+} (Tb^{3+} and Eu^{3+}) as green and red light sources, which can be excited by NUV light to produce emission in the visible light region. Based on the above advantages, the combination of $NaGdF_4$:Ln^{3+} and CQDs is expected to produce unexpectedly excellent white light emission.

Reducing metals to a single atom scale is an effective strategy to improve metal utilization efficiency [31–36]. Therefore, single atom material has attracted great attention as a cutting-edge material [37]. Among them, RE single atom has caused extensive research by researchers. The unique structure of RE metals on a single atomic scale can endow the material with an unexpected performance, such as good dispersion, great atom utilization, unique atomic structure, and special electronic properties [38]. Atomically dispersed metal atoms are usually anchored to a specific carrier through chemical bonding with neighboring atoms. For example, g-C_3N_4 and MOFs can effectively anchor single atoms [39–43]. However, these RE single atom materials with excellent properties are mostly used in catalysis research, and there are very few applications in the field of fluorescent materials. For clarity, a comparison of the contents of different references concerning RE single atom materials is listed in Table S1 in the Electronic Supplementary Material (ESM).

In this work, a novel RE single atom doped composite luminescence material ($NaGdF_4$:Tb^{3+}/Eu^{3+}@C:N/Eu^{3+}) with full-color tunable emission as well as high thermal and light stability was reported. The C:N/Eu^{3+} with enhanced luminescence was composited as a blue fluorescent layer on the surface of the $NaGdF_4$:Tb^{3+}/Eu^{3+} core with dual emission centers, forming a novel composite material emitting white light. The density functional theory (DFT) was used to optimize the structures of the C:N/Eu^{3+} and $NaGdF_4$:Tb^{3+}/Eu^{3+}, and calculate the work function, optical properties, and charge density difference. The synthesized $NaGdF_4$:Tb^{3+}/Eu^{3+}@C:N/Eu^{3+} not only has good stability, high luminous performance, excellent color quality, and visual effects but also can simultaneously emit red, green, and blue light, which successfully solves the issues of WLED multi-component phosphors. We can not only construct WLEDs with CQDs:N/Eu^{3+} and $NaGdF_4$:Tb^{3+}/Eu^{3+}, but also directly construct WLED devices with the $NaGdF_4$:Tb^{3+}/Eu^{3+}@C:N/Eu^{3+} single composite material. Interestingly, the NUV-pumped single $NaGdF_4$:Tb^{3+}/Eu^{3+}@C:N/Eu^{3+} phosphor-based high-quality WLED devices with a high CRI of 95 and an ideal CCT of 4,688 K were obtained. As a tunable full-color luminescent material, the RE single atom based $NaGdF_4$:Tb^{3+}/Eu^{3+}@C:N/Eu^{3+} has broad prospects in the application of WLED devices.

2 Results and discussion

2.1 Design principles of overall work

Based on the above considerations, we have designed an efficient fluorescent composite, which has the advantages of both C:N/Eu^{3+} and $NaGdF_4$:Ln^{3+} materials, as shown in Scheme 1. Firstly, $NaGdF_4$:Ln^{3+} nanoparticles were synthesized by the solvothermal method, and then $NaGdF_4$:Ln^{3+} was added to the precursor solution of C:N/Eu^{3+}. Finally, the C:N/Eu^{3+} layer was coated on the $NaGdF_4$:Ln^{3+} surface to form $NaGdF_4$:Tb^{3+}/Eu^{3+}@C:N/Eu^{3+} core–shell composites through further hydrothermal reaction (Scheme 1(a)). As we predict, the synthesized $NaGdF_4$:Tb^{3+}/Eu^{3+}@C:N/Eu^{3+} can simultaneously emit full-color light (including blue, red, green, and white light), and energy transfer exists in the composite material (Scheme 1(b)). To verify the application of the obtained composite single-phase $NaGdF_4$:Tb^{3+}/Eu^{3+}@C:N/Eu^{3+} white light-emitting material in WLEDs, the NUV-LED chips were used to excite the material to obtain WLED devices, and the performance of the WLEDs was studied (Scheme 1(c)). The specific synthesis method and operation steps are shown in the experimental part.

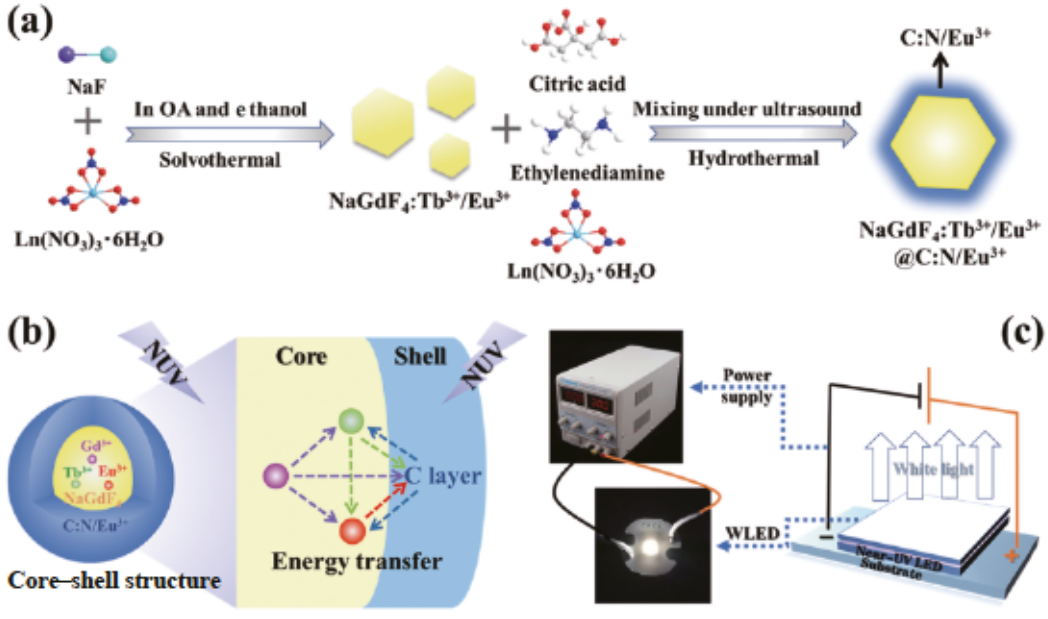

Scheme 1 Schematic diagrams. (a) The synthesis process of $NaGdF_4$:Tb^{3+}/Eu^{3+}@C:N/Eu^{3+}. (b) Energy transfer process between different Ln^{3+} ions and C layer. (c) The schematics and photographs of WLED devices.

2.2 DFT calculation and discussion

We performed DFT calculations on the relevant materials involved in this study. Figures 1(a)–1(d) and Fig. S1 in the ESM show the optimized geometric structures of C_{61} (C), $C_{60}Eu_4$ (CE), $C_{60}N_4$ (CN), and $C_{54}N_4Eu_4$ (CNE). The results show that N can easily replace C and form a stable $C_{60}N_4$ structure after optimization. However, the Eu^{3+} ion cannot simply replace the position of C to form a stable $C_{60}Eu_4$ (or $C_{54}N_4Eu_4$) structure. First, Eu^{3+} replaces the position of C before optimization. And then, Eu^{3+} leaves the original position after optimization because the radius of Eu^{3+} is much larger than that of C, resulting in several defects in the (001) surface of $C_{60}Eu_4$ (or $C_{54}N_4Eu_4$). In addition, when Eu^{3+} is located in the middle of the carbon layer, the energy is the lowest; therefore, the structure of $C_{60}Eu_4$-b in Fig. S1(b) in the ESM is the most stable. Thus, C is more favorable for anchoring Eu^{3+} single atoms rather than doping and replacing C atoms, which is consistent with our previous results [37].

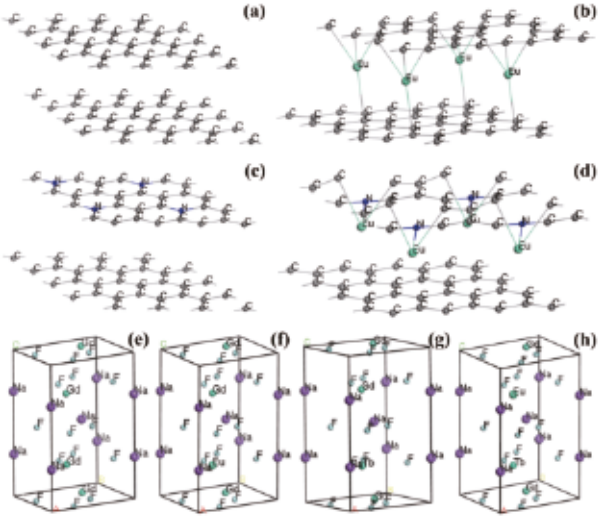

Figure 1 Optimized geometric structures of samples: (a) C_{60}, (b) $C_{60}Eu_4$, (c) $C_{60}N_4$, (d) $C_{54}N_4Eu_4$, (e) $Na_3Gd_3F_{12}$, (f) $Na_3Gd_2EuF_{12}$, (g) $Na_3Gd_2TbF_{12}$, and (h) $Na_3GdEuTbF_{12}$.

Figures 1(e)–1(h) show the optimized geometric structures of $Na_3Gd_3F_{12}$ (NGF), $Na_3Gd_2EuF_{12}$, $Na_3Gd_2TbF_{12}$ (NGFT), and $Na_3GdEuTbF_{12}$ (NGFTE). The corresponding cell parameters are shown in Table S2 in the ESM. The lattice parameters change slightly with the different kinds of RE ions, which can be attributed to the different radii of RE ions. The band structure (BS) and density of states (DOS) of $Na_3Gd_3F_{12}$ are shown in Fig. S2 in the ESM, and the bandgap energy of $Na_3Gd_3F_{12}$ is 7.022 eV. After doping with Eu^{3+} (or Tb^{3+}), the bandgap becomes very narrow, because the rich 4f energy levels of Eu^{3+} (or Tb^{3+}) form rich impurity energy levels in $Na_3Gd_3F_{12}$ (Figs. S3 and S4 in the ESM).

Figure 2 shows the theoretical simulation of optical properties for C, CE, CN, CNE, $Na_3Gd_3F_{12}$, NGFE, NGFT, NGFTE, and NGFTE-CNE heterojunction. In particular, the dielectric function is related to the electronic transition and electronic structure in the crystal and can reflect the band structure and optical properties of the materials. The imaginary part of the dielectric function describes the actual transition between the occupied state and the unoccupied state. The results indicate that the optical properties of C, CE, CN, CNE, NGF, NGFE, NGFT, NGFTE, are different. Therefore, we can obtain fluorescent materials with almost any desired spectral property by reasonably constructing NGFTE-CNE heterojunctions, which can also be used in various optoelectronic devices including WLEDs.

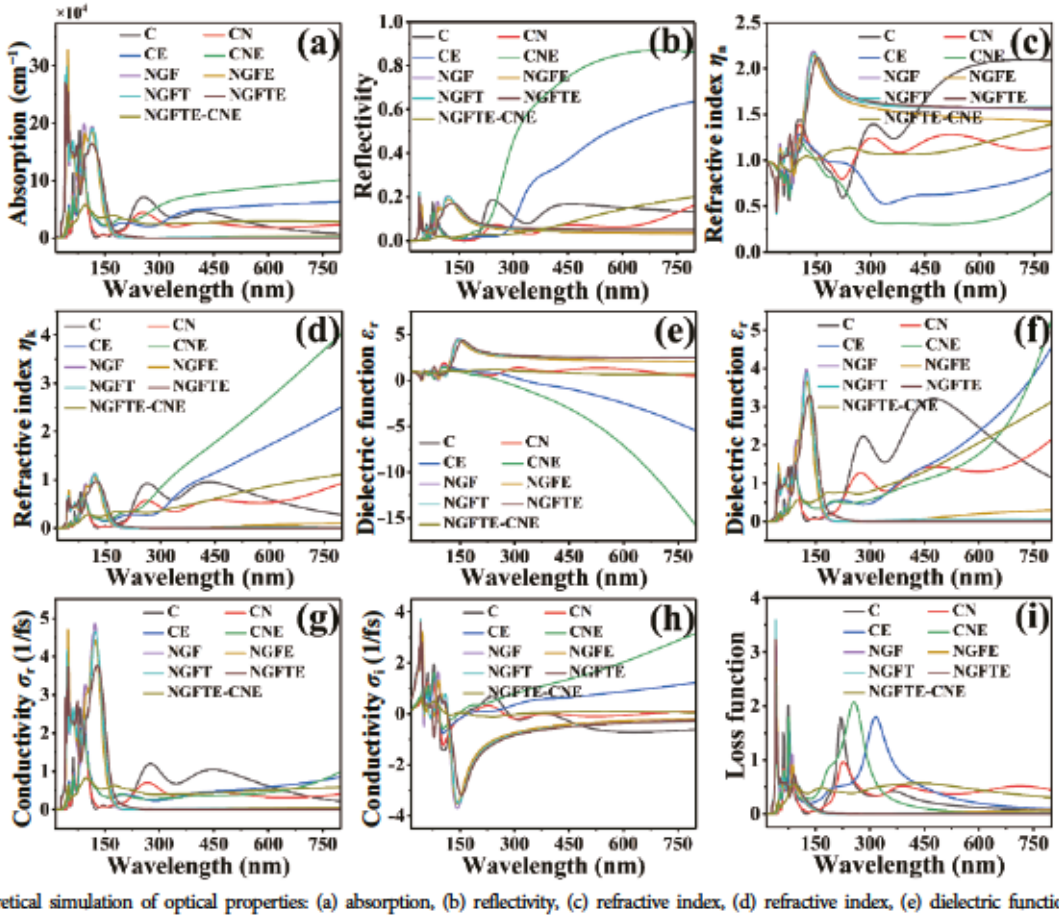

Figure 2 Theoretical simulation of optical properties: (a) absorption, (b) reflectivity, (c) refractive index, (d) refractive index, (e) dielectric function, (f) dielectric function, (g) conductivity, (h) conductivity, and (i) loss function spectra.

Figures 3(a)–3(j) show the deformation charge densities of C, CE, CN, CNE, NGF, NGFE, NGFT, NGFTE, NGF-C heterojunction, and NGFTE-CNE heterojunction. Herein, the blue area shows that the electron density is increasing, and on the contrary, the yellow area is decreasing. Figure 3(k) shows the corresponding Fermi levels, vacuum level, and work functions. The Fermi level changes after N or Eu doping. Herein, the increase of the Fermi level indicates the increase of electron concentration. Besides, the values of work functions are 6.102, 3.957, 3.733, and 3.308 eV for the (001) crystal planes of C, CE, CN, and CNE, respectively. The values of work functions are 4.448, 4.698, 4.796, and 5.511 eV for the (001) crystal planes of NGF, NGFE, NGFT, and NGFTE, respectively. The values of work functions are 4.485 and 4.359 eV for the (001) crystal planes of NGF-C, and NGFTE-CNE heterojunction, respectively. The values of the work functions of C decrease after N (or Eu) doping, while the values of the work functions of NGF increase after Tb (or Eu) doping. Especially, the change of work functions between NGF-C and NGFTE-CNE heterojunction directly affects the energy transfer between NGFTE and CNE in NGFTE-CNE heterojunction, so the luminescent performance of the NGFTE-CNE heterojunction can be further adjusted, which will be discussed in detail later.

2.3 Structural and morphological characterizations

The detailed synthesis information, sample abbreviation, and Commission Internationale de l'éclairage (CIE) chromaticity coordinates are listed in Tables S3 to S6 in the ESM.

Figure S5 in the ESM shows the X-ray diffraction (XRD) patterns of CQDs:3N/5Eu^{3+}, NGFTE-2.5@CNE, and $NaGdF_4$:15%Tb^{3+}/1.5%Eu^{3+}. A broad diffraction peak near 24° is attributed to the reflection of the (002) crystal plane of the graphite structure, indicating that the CQDs have some carbon materials with graphite sp^2 carbon atoms (Fig. S5(a) in the ESM). The XRD patterns of $NaGdF_4$:15%Tb^{3+}/1.5%Eu^{3+} and NGFTE-2.5@CNE in Figs. S5(b) and S5(c) in the ESM indicate that all diffraction peaks of $NaGdF_4$:15%Tb^{3+}/1.5%Eu^{3+} can be indexed to hexagonal phase β-$NaGdF_4$ (JCPDS No. 27-0699). Please note that the carbon layer almost does not cause the shift of the $NaGdF_4$ diffraction peaks.

The transmission electron microscopy (TEM) and high-resolution TEM (HRTEM) images of CQDs:3N/5Eu^{3+} (Figs. 4(a) and 4(b)) show that the CQDs particles have good dispersibility and are nearly spherical, with a particle size of about 5 nm. The lattice fringe spacing of the CQDs:3N/5Eu^{3+} is about 0.21 nm, corresponding to the typical graphite phase (100) crystal plane, confirming the successful synthesis of CQDs:3N/5Eu^{3+}. Figures 4(c) and 4(d) are the TEM and HRTEM images of the core–shell structure of NGFTE-2.5@CNE, respectively. The combination of $NaGdF_4$:Tb^{3+}/Eu^{3+} and CQDs:N/Eu^{3+} requires a hydrothermal process. During the hydrothermal process, CQDs:N/Eu^{3+} self-assembles on the surface of $NaGdF_4$:Tb^{3+}/Eu^{3+}, thus forming a carbon layer (C:N/Eu^{3+}). The outer shell layer is about 6 nm thick, and the obvious shell structure corresponds to the carbon layer. The lattice fringe spacing of the core is 0.52 nm, corresponding to the (100) crystal plane of β-$NaGdF_4$. To further explore the core–shell structure and surface state of the composite material, high-angle annular dark-field scanning TEM (HAADF-STEM) measurements were also carried out, as shown in Figs. 4(e) and 4(f). It is worth noting that isolated bright spots are observed on the surface of the material, which indicates that Eu^{3+} is successfully doped in CQDs and forms a RE single atom structure in the carbon layer. The HAADF-STEM element mapping images in Figs. 4(g) and 4(h) show the presence and uniform distribution of elements in the composite sample. Our previous results also show that the C and N elements can anchor RE single atoms very well [37]. At present, the coordination of a single atom is characterized by synchrotron radiation technology, but the synchrotron radiation test cannot be performed due to the low concentration of RE atom in our samples.

The compositions of the CQDs:3N/5Eu^{3+}, $NaGdF_4$:15%Tb^{3+}/

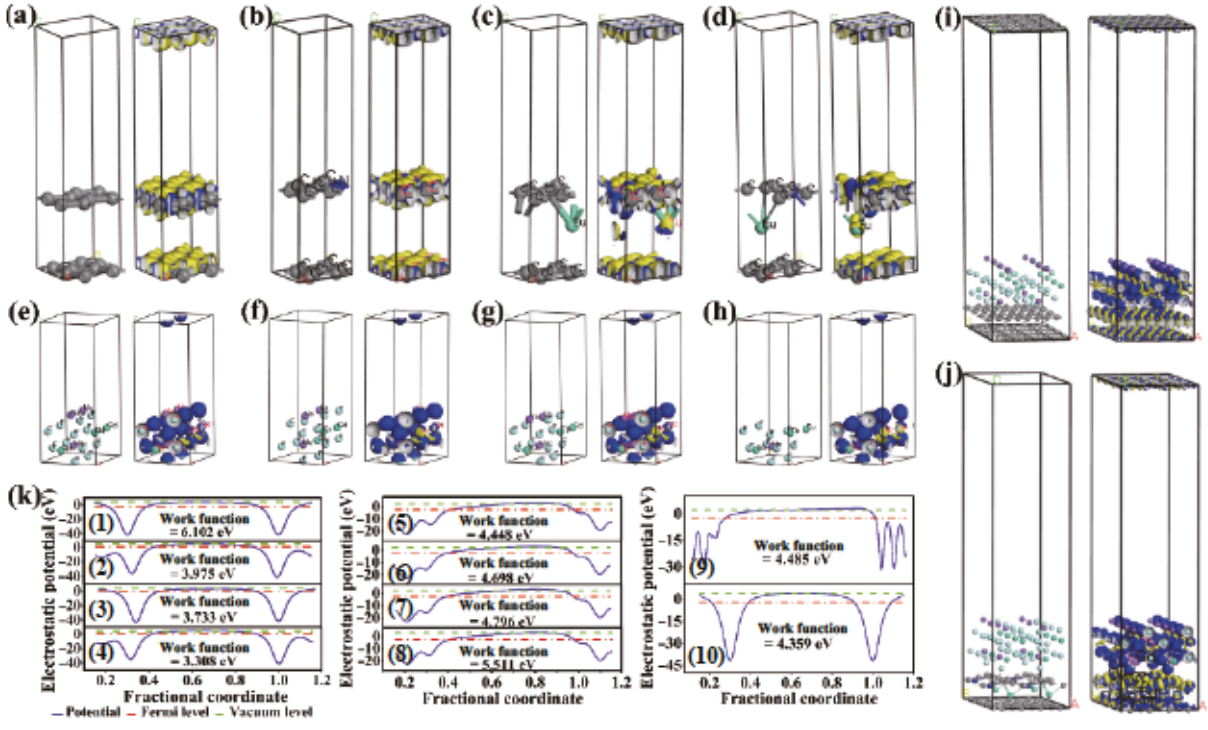

Figure 3 Deformation charge density, calculated Fermi levels, vacuum level, and work functions. The deformation charge densities of (a) C, (b) CE, (c) CN, (d) CNE, (e) NGF, (f) NGFE, (g) NGFT, (h) NGFTE, (i) NGF-C heterojunction, and (j) NGFTE-CNE heterojunction (the blue area shows that the electron density is increasing, on the contrary, the yellow area is decreasing). (k) Calculated Fermi levels, vacuum level, and work functions of (1) C, (2) CE, (3) CN, (4) CNE, (5) NGF, (6) NGFE, (7) NGFT, (8) NGFTE, (9) NGF-C heterojunction, and (10) NGFTE-CNE heterojunction.

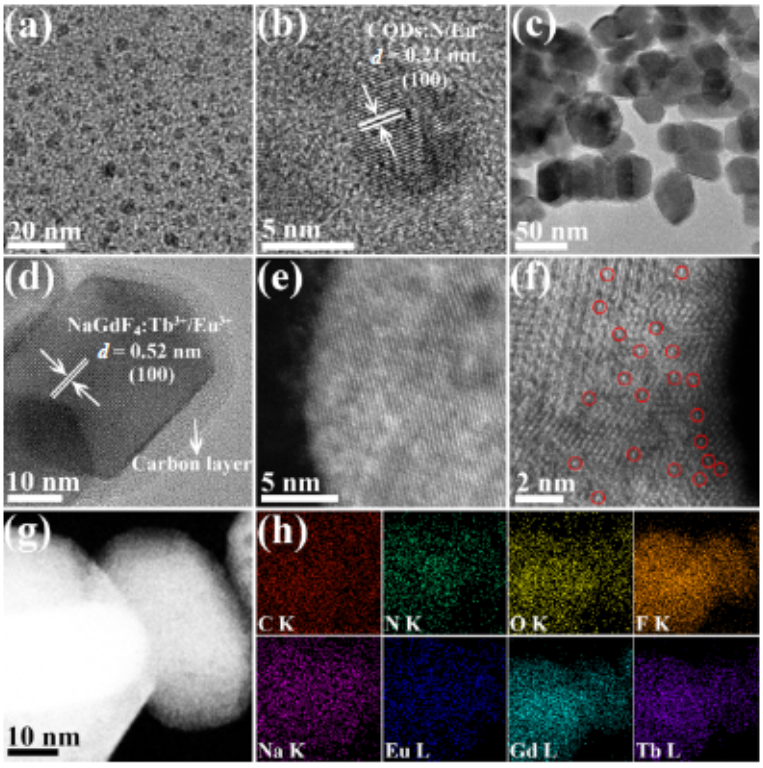

Figure 4 Morphological characterization of samples. TEM and HRTEM images of ((a) and (b)) CQDs:3N/5Eu^{3+} and ((c) and (d)) NaGdF$_4$:15%Tb^{3+}/1.5%Eu^{3+}@C:3N/5Eu^{3+}. (e) and (f) STEM images of NaGdF$_4$:15%Tb^{3+}/1.5%Eu^{3+}@C:3N/5Eu^{3+}. (g) and (h) The elemental mapping images of C, N, O, F, Na, Eu, Gd, and Tb in NaGdF$_4$:15%Tb^{3+}/1.5%Eu^{3+}@C:3N/5Eu^{3+}.

1.5%Eu^{3+}, and NGFTE-2.5@CNE nanocomposites were determined by using energy dispersive X-ray (EDX) analysis, as shown in Fig. S6(a)–S6(c) in the ESM. The elements in the NGFTE-2.5@CNE nanocomposites are Na, F, Gd, Tb, Eu, C, O, and N, which indicates that C:3N/5Eu^{3+} and NaGdF$_4$:15%Tb^{3+}/1.5%Eu^{3+} co-exist in the NGFTE-2.5@CNE nanocomposites.

Figure S7 in the ESM shows the Fourier transform infrared (FT-IR) spectra of CQDs:3N/5Eu^{3+}, NaGdF$_4$:15%Tb^{3+}/1.5%Eu^{3+}, and NGFTE-2.5@CNE, which are used to identify the surface functional groups of nanomaterials. In the FT-IR spectrum of NaGdF$_4$:15%Tb^{3+}/1.5%Eu^{3+}, the bands at 2,928 and 2,857 cm^{-1} are derived from the antisymmetric and symmetric aliphatic stretching vibrations of methylene groups (–CH$_2$) in the oleic acid molecule [44]. The sharp peak around 3,618 cm^{-1} is attributed to the –OH stretching vibration of ethanol. The broad band between 3,000 and 3,500 cm^{-1} is determined to be the stretching vibration of H–O–H and N–H. In addition, the peaks at less than 600 cm^{-1} correspond to Gd–F [45]. It is worth noting that CQDs:3N/5Eu^{3+} and NGFTE-2.5@CNE show some similar characteristic peaks. For NGFTE-2.5@CNE, the peak near 1,583 cm^{-1} is attributed to the tensile vibration of C=O and C=C, and the peak centered at 1,379 cm^{-1} is mainly designated as C–N and N–H groups [46]. The peak at 850 cm^{-1} is derived from CH$_3$–N. The above several similar characteristic peaks indicate that there are carboxyl groups on the surface of CQDs:3N/5Eu^{3+} and NGFTE-2.5@CNE, and nitrogen may be successfully doped on the surface of CQDs:3N/5Eu^{3+} to form stable chemical bonds, which also proves the carbon layer coating on the surface of NaGdF$_4$:15%Tb^{3+}/1.5%Eu^{3+}.

The UV–vis absorption spectra of the samples are shown in Fig. S8 in the ESM. The absorption range of NaGdF$_4$:15%Tb^{3+}/1.5%Eu^{3+} is mainly in the UV region. And the absorption peaks at 273 and 395 nm are caused by doping RE ions [22]. The co-doping of RE ions greatly enhances the absorption intensity. The UV–vis absorption spectrum of CQDs:3N/5Eu^{3+} shows two absorption peaks at 245 and 360 nm, which can be attributed to the $\pi\rightarrow\pi^*$ transition of C=C bond and the $n\rightarrow\pi^*$ transition of C=O bond [46]. This can prove that the carboxyl functional groups exist on the surface of co-doped CQDs. This result is consistent with the FT-IR spectra discussed above. When CQDs:3N/5Eu^{3+} is coated on the surface of NaGdF$_4$:15%Tb^{3+}/1.5%Eu^{3+} to form a carbon layer, the absorption peak range of the composite sample moves toward the visible light region. The absorption peak of the composite sample at around 360 nm is similar to that of CQDs:3N/5Eu^{3+}, and the absorption intensity in the visible light region greater than 400 nm is significantly enhanced. This can also indicate the presence of the carbon layer on the surface of NaGdF$_4$:15%Tb^{3+}/1.5%Eu^{3+}.

The thermogravimetric analysis (TGA) was performed between room temperature and 800 ℃, and the heating rate in the air was 10 ℃/min, as shown in Fig. S9 in the ESM. The weight loss of the sample NGFTE-2.5@CNE between 200 and 800 ℃ is about 9%, indicating that the sample has relatively good stability. As we all know, NaGdF$_4$ can be oxidized to oxides under the same test conditions, and there is usually little weight loss. Thus, the main cause of weight loss may be due to the decomposition of the carbon layer as shells at high temperatures. N_2 adsorption–desorption isotherms were performed to determine the surface area of the samples, as shown in Fig. S10 in the ESM. The Brunauer–Emmett–Teller (BET) surface area are 20.8412 and 12.4624 m^2/g for NaGdF$_4$:15%Tb^{3+}/1.5%Eu^{3+} and NGFTE-2.5@CNE, respectively. The specific surface area of the composite nanoparticles becomes smaller, in line with expectations. This means that the carbon layer is coated on the surface of the NaGdF$_4$:15%Tb^{3+}/1.5%Eu^{3+}.

The X-ray photoelectron spectroscopy (XPS) spectra of CQDs:3N/5Eu^{3+}, NGFTE-2.5@CNE, and NaGdF$_4$:15%Tb^{3+}/1.5%Eu^{3+} are shown in Fig. S11(a) in the ESM. The signals contained in the XPS spectrum of NGFTE-2.5@CNE can be attributed to the existence of Na, F, Eu, Gd, Tb, C, N, and O. The above results indicate that the surface of the

$NaGdF_4$:15%Tb^{3+}/1.5%Eu^{3+} is coated with a carbon layer. Figures S11(b) and S11(c) in the ESM show the high-resolution C 1s spectra of CQDs:3N/5Eu^{3+} and NGFTE-2.5@CNE, respectively. The high-resolution C 1s spectra of CQDs:3N/5Eu^{3+} show that the four peaks are located at 284.6 (C–C/C=C), 286.1 (C–O/C–N), 288.6 (C=O), and 290.1 eV (the graphitized structure $\pi \rightarrow \pi^*$ transition), respectively. Compared with CQDs:3N/5Eu^{3+}, the positions of C 1s peaks of NGFTE-2.5@CNE shift, indicating that there is electron transfer between C and N on the surface, which is consistent with the results of the later spectral analysis.

2.4 Optical performance

The photoluminescence (PL) emission intensity of CQDs is often affected by the surface state because the surface defects will change the energy level structure to a certain extent, thereby affecting the transition of electrons between different energy levels. The doping of atoms affects the surface functionalization and defect state adjustment, which can further affect the PL intensity of the CQDs. The results show that the luminescence intensity can effectively be enhanced by doping N and Eu^{3+} in CQDs. As shown in Fig. 5(a), the emission intensity of CQDs:Eu^{3+} under 361 nm excitation is significantly stronger than that of pure CQDs, which can be attributed that the Eu^{3+} doping in the CQDs can adjust the surface state defects, thereby increasing the luminous intensity of the CQDs. In addition, the effective doping of N atoms in CQDs will also be of benefit to improve the property of CQDs and significantly increase their emission intensity (Fig. 5(b)). And then, the influence of the Eu^{3+} concentration on the fluorescence property of CQDs:3N/xEu^{3+} was studied. The corresponding emission spectra of the CQDs:3N/xEu^{3+} doped with different Eu^{3+} concentrations are shown in Fig. 5(c). The characteristic broad emission peaks at 443 nm of CQDs were obtained upon 384 nm excitation. The emission of the CQDs:3N/xEu^{3+} increases gradually with increasing Eu^{3+} concentrations from 0% to 5% and then decreases at higher Eu^{3+} concentrations. The corresponding excitation spectra (λ_{ex} = 443 nm) of CQDs:xN and CQDs:3N/xEu^{3+} are shown in Fig. S12 in the ESM. And the excitation peaks of CQDs:xN and CQDs:3N/xEu^{3+} shift slightly. The result shows that when N/Eu^{3+} is co-doped, the luminescence of CQDs is further enhanced.

In general, the emission color of the Tb^{3+} and Eu^{3+} co-doped samples can be changed from green to green-yellow, yellow, orange-red, and red by adjusting the relative doping concentration of the activator ions under single wavelength excitation. Therefore,

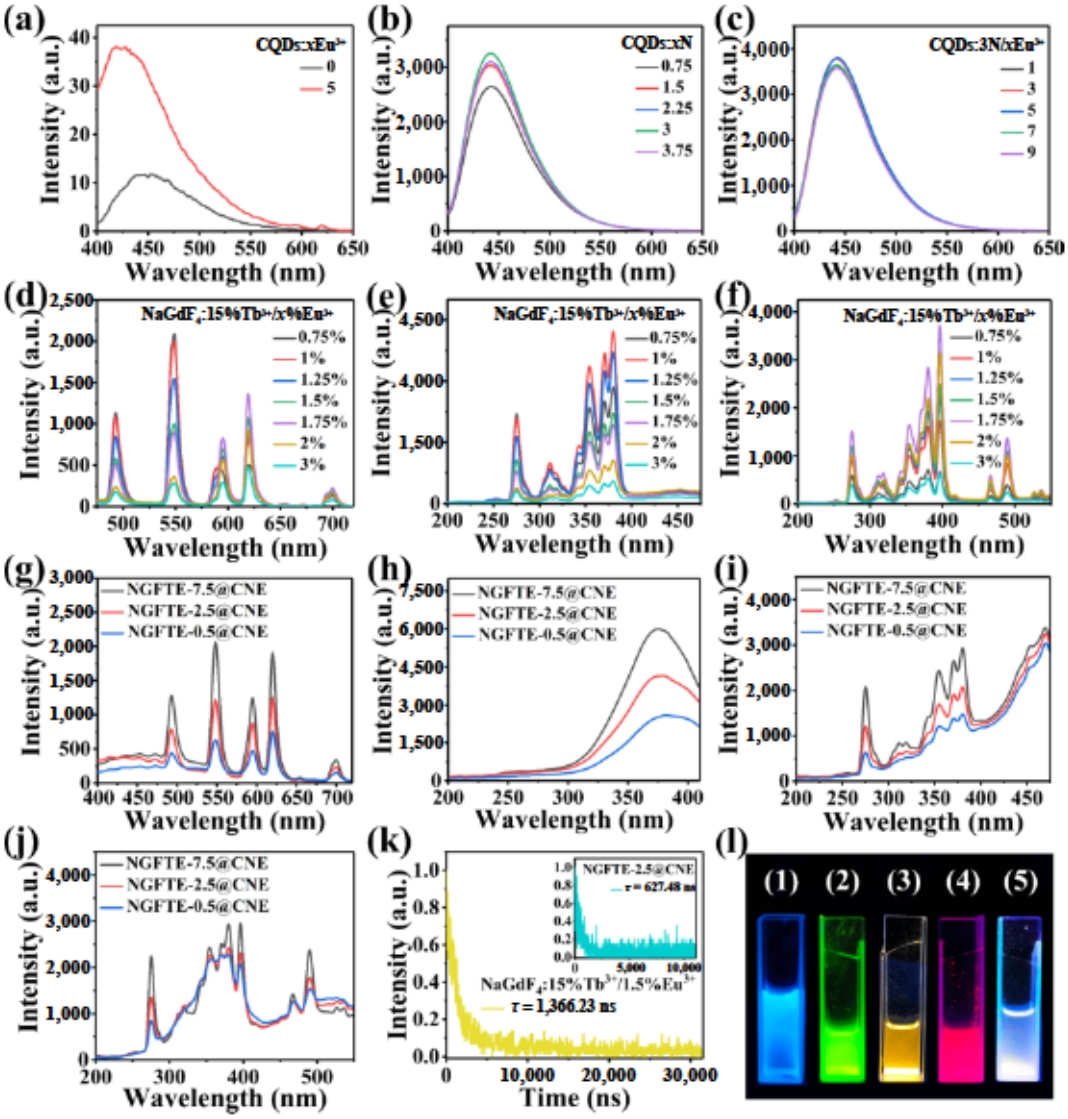

Figure 5 Optical performance of samples. (a) Emission (λ_{ex} = 361 nm) spectra of CQDs and CQDs:5Eu^{3+}. (b) Emission (λ_{ex} = 384 nm) spectra of CQDs:xN. (c) Emission (λ_{ex} = 384 nm) spectra of CQDs:3N/xEu^{3+}. (d)–(f) Emission (λ_{ex} = 275 nm) and excitation (λ_{em} = 548 and 619 nm) spectra of $NaGdF_4$:15%Tb^{3+}/xEu^{3+}. (g)–(j) Emission (λ_{ex} = 275 nm) and excitation (λ_{em} = 443, 548, and 619 nm) spectra of $NaGdF_4$:Tb^{3+}/Eu^{3+}@C:N/Eu^{3+} with different mass ratios of CQDs:N/Eu^{3+} and $NaGdF_4$:Tb^{3+}/Eu^{3+}. (k) Luminescence decay curves of the $NaGdF_4$:Tb^{3+}/Eu^{3+} and $NaGdF_4$:Tb^{3+}/Eu^{3+}@C:N/Eu^{3+}. (l) Luminescence photos of samples in the liquid under NUV light.

to find $NaGdF_4$ nanocrystals with the best ratio of green and red emission and suitable for the next WLED application research, three kinds of doping modes for relevant verification and spectral analysis were carried out. Compared with the spectra of $NaGdF_4$:Tb^{3+} or $NaGdF_4$:Eu^{3+} (Figs. S13(a)–S13(d)) in the ESM), the positions of the emission and excitation peaks of Eu^{3+} or Tb^{3+} do not change significantly. The Gd^{3+} component in RE fluoride nanocrystals helps to transfer energy from the host lattice to the luminous center (Tb^{3+} and Eu^{3+}). It can be seen from the excitation and emission spectra that there is an obvious energy transfer phenomenon among Gd^{3+}, Tb^{3+}, and Eu^{3+}. Due to the presence of Gd^{3+}, the Tb^{3+} and Eu^{3+} can be excited at 275 nm, and the emission peaks of Tb^{3+} and Eu^{3+} are narrow and strong. It is worth noting that regardless of the Tb^{3+}/Eu^{3+} doping ratio, the emission intensity of $NaGdF_4$:Tb^{3+}/Eu^{3+} is lower than those of the single-doped samples, which is also evidence of energy transfer. To prove the change of the symmetry of the local environment around Eu^{3+}, the Judd-Oflet (J-O) parameters Ω_2 of $NaGdF_4$:Eu^{3+} with different Eu^{3+} concentrations from emission spectra were calculated (Table S7 in the ESM). The values of Ω_2 of $NaGdF_4$:Eu^{3+} increase with increasing Eu^{3+} concentration, demonstrating the symmetry of the local environment around Eu^{3+} ions decreases with increasing Eu^{3+} concentration.

In the emission spectra of $NaGdF_4$:Tb^{3+}, the maximum emission intensity is obtained when the concentration of Tb^{3+} is 15%. Therefore, for the Tb^{3+} and Eu^{3+} co-doped $NaGdF_4$ nanocrystals, the doping ratio of Tb^{3+} was first fixed to 15%, and the influence of Eu^{3+} concentration on the luminescence of Tb^{3+}/Eu^{3+} co-doped $NaGdF_4$ was explored. As shown in Fig. 5(d), obvious emission at 493, 548, 589, 594, 619, 624, 654, and 700 nm can be observed, which is mainly due to the $^5D_0 \rightarrow {}^7F_J$ (J = 1–4) transition of Eu^{3+} and the $^5D_4 \rightarrow {}^7F_J$ (J = 6–3) transition of Tb^{3+}. Figures 5(e) and 5(f) show the excitation spectra of $NaGdF_4$:Tb^{3+}/Eu^{3+} by monitoring the emission at 548 and 619 nm. The excitation peaks at 275 and 312 nm correspond to the $^8S_{7/2} \rightarrow {}^6I_J$ and $^8S_{7/2} \rightarrow {}^6P_J$ energy level transitions of the host Gd^{3+}, respectively. The excitation peaks in the range of 330–400 nm correspond to the transitions of Tb^{3+} and Eu^{3+}. Monitoring at 619 nm, the excitation peak of Eu^{3+} overlaps with the excitation peak of Tb^{3+} partly. Compared with the excitation spectrum by monitoring 548 nm (Tb^{3+}) emission, there is a particularly strong Eu^{3+} characteristic excitation peak at 396 nm. It can be seen from the excitation spectra that Tb^{3+} and Eu^{3+} can be simultaneously excited at 275, 312, 319, 343, 354, 371, and 380 nm. The emission spectra show that when the Tb^{3+} concentration is fixed at 15%, increasing the Eu^{3+} concentration has a greater impact on the Tb^{3+} luminescence. With increasing of Eu^{3+} concentration, the emission peak of Eu^{3+} gradually increases, and the emission peak of Tb^{3+} gradually decreases. The energy transfer among Gd^{3+}, Tb^{3+}, and Eu^{3+} is obvious. Until the concentrations of Tb^{3+} and Eu^{3+} separately reach 15% and 2%, the concentration quenching effect begins to appear. The above results indicate that 15% Tb^{3+} and 1%–2% Eu^{3+} may be suitable for obtaining appropriate ratios of green and red emissions of $NaGdF_4$. The calculated J-O parameters and the emission peak area ratios of $^5D_0$-$^7F_2$/$^5D_0$-$^7F_1$ from the emission spectra of $NaGdF_4$:15%Tb^{3+}/$x$$Eu^{3+}$ with different Eu^{3+} concentrations are shown in Table S8 in the ESM. The values of Ω_2 of $NaGdF_4$:15%Tb^{3+}/$x$$Eu^{3+}$ increase with increasing Eu^{3+} concentration.

In addition, the effect of Tb^{3+} doping concentration on the luminescence of $NaGdF_4$:1%Eu^{3+}/$x$$Tb^{3+}$ is also explored (Figs. S14(a)–S14(c) in the ESM). When Tb^{3+} and Eu^{3+} are less mixed into the host matrix (less than 5%), the excitation peak at 275 nm dominates. As the doped Tb^{3+}/Eu^{3+} concentration increases, the luminescence intensity increases, and at a co-doping concentration of 15% Tb^{3+} and 1% Eu^{3+}, the strongest emission is observed in $NaGdF_4$:Tb^{3+}/Eu^{3+}. The relevant J-O parameters are shown in Table S9 in the ESM. We also explored the luminescence of $NaGdF_4$:$x$$Tb^{3+}$/y$Eu^{3+}$ (Figs. S14(d)–S14(f) in the ESM). When the concentration of Gd^{3+} in the matrix is fixed, the phenomenon of energy transfer becomes more obvious. With the decrease in Tb^{3+} concentration and the increase in Eu^{3+} concentration, the energy transfer from Tb^{3+} to Eu^{3+} gradually increases, which sharply increases the Eu^{3+} emission at 595 and 619 nm, and produces a much stronger emission than the single-Eu^{3+} doped $NaGdF_4$. The relevant J-O parameters are shown in Table S10 in the ESM.

In order to study the luminescence properties of $NaGdF_4$:15%Tb^{3+}/1.5%Eu^{3+} and CQDs:3N/5Eu^{3+} composite materials, we carried out two control methods to control the ratio of the two materials. In the synthesis process of control method 1, the mass of C:3N/5Eu^{3+} precursor was fixed, and then a different mass of $NaGdF_4$:15%Tb^{3+}/1.5%Eu^{3+} was added to the precursor solution to further synthesize $NaGdF_4$:15%Tb^{3+}/1.5%Eu^{3+}-x@C:3N/5Eu^{3+} (NGFTE-x@CNE). In the synthesis process of control method 2, $NaGdF_4$:15%Tb^{3+}/1.5%Eu^{3+} with fixed mass was added to the different masses of C:3N/5Eu^{3+} precursor solution, and then $NaGdF_4$:15%Tb^{3+}/1.5%Eu^{3+}@C:3N/5Eu^{3+}-x (NGFTE@CNE-x) was further synthesized. Figure 5(g) shows the emission spectra of NGFTE-x@CNE with different mass ratios of C:3N/5Eu^{3+} and $NaGdF_4$:15%Tb^{3+}/1.5%Eu^{3+}. The emission peaks of C:3N/5Eu^{3+} and $NaGdF_4$:15%Tb^{3+}/1.5%Eu^{3+} can be observed intuitively. By a lot of experimental optimizations, the synthesized composite sample has almost standard white emission on the main CCT line, as shown in Fig. S15(a) in the ESM. When the coating amount of C:3N/5Eu^{3+} is large, the blue light of C:3N/5Eu^{3+} is stronger, and it is easy to obtain neutral light or cool white light. When the amount of C:3N/5Eu^{3+} is fixed, the luminescence intensity of the composite sample changes significantly with the amount of $NaGdF_4$:15%Tb^{3+}/1.5%Eu^{3+}. When the addition amount of $NaGdF_4$:15%Tb^{3+}/1.5%Eu^{3+} is large, the C:3N/5Eu^{3+} coated on the surface of $NaGdF_4$:15%Tb^{3+}/1.5%Eu^{3+} is relatively less; the composite material emits better luminous intensity at this time, and the emission of Tb^{3+}/Eu^{3+} ions (red and green light) is dominant. For the excitation spectra, a broad excitation band of 200–400 nm is observed (Fig. 5(h)), which is similar to the excitation spectrum of CQDs:3N/5Eu^{3+} (Fig. S12(b) in the ESM). Figures 5(i) and 5(j) correspond to the excitation spectra of NGFTE-x@CNE monitored at 548 and 619 nm, respectively. The main narrow excitation peaks are consistent with the characteristic excitation peaks of Tb^{3+} and Eu^{3+} of $NaGdF_4$. It is worth noting that a broad excitation band appears at > 400 nm, which can be used as evidence for energy transfer from C:3N/5Eu^{3+} to $NaGdF_4$:15%Tb^{3+}/1.5%Eu^{3+}. It can be seen from the excitation spectra of Tb^{3+} and Eu^{3+} that the energy transfer from C:3N/5Eu^{3+} to Tb^{3+} is more than that from C:3N/5Eu^{3+} to Eu^{3+}. The calculated J-O parameters and the emission peak area ratios of $^5D_0$-$^7F_2$/$^5D_0$-$^7F_1$ from the emission spectra of NGFTE-x@CNE with different mass ratios of C:3N/5Eu^{3+} and $NaGdF_4$:15%Tb^{3+}/1.5%Eu^{3+} are shown in Table S11 in the ESM. The values of Ω_2 of NGFTE-x@CNE are changed.

Figure S16 in the ESM shows the emission and excitation spectra of composite samples with fixed $NaGdF_4$:15%Tb^{3+}/1.5%Eu^{3+} mass and different C:3N/5Eu^{3+}. Different from the previous mode, when the amount of $NaGdF_4$:15%Tb^{3+}/1.5%Eu^{3+} is fixed, the emission intensity of Tb^{3+}/Eu^{3+} in the composite sample changes less. In this case, the blue emission intensity of C:3N/5Eu^{3+} is easier to adjust. By adding more C:3N/5Eu^{3+} precursors, higher blue emission of C:3N/5Eu^{3+} can be obtained. The CIE chromaticity coordinate (0.333, 0.336) close to the standard white light emission was obtained (Fig.

S15(b) in the ESM). The calculated J-O parameters and the emission peak area ratios of $^5D_0$-$^7F_2$/$^5D_0$-$^7F_1$ from the emission spectra in Fig. S16(a) are shown in Table S12 in the ESM. The values of Ω_2 are almost unchanged.

In addition, it should be noted that the broad excitation band of C:3N/5Eu^{3+} overlaps with the excitation peaks of Ln^{3+} ions. Therefore, there are multiple kinds of single-wavelength excitation processes, and NaGdF$_4$:Tb^{3+}/Eu^{3+} and C:3N/5Eu^{3+} will be excited simultaneously. From the emission spectrum of NGFTE@CNE-1.5 (Fig. S17 in the ESM), it can be seen that as the excitation wavelength increases, the blue emission intensity from C:3N/5Eu^{3+} will increase sharply and the sample mainly emits blue light, which will lead to high CCT and low CRI. Therefore, although it is possible to simultaneously excite NaGdF$_4$:15%Tb^{3+}/1.5%Eu^{3+} and C:3N/5Eu^{3+} with multiple excitation wavelengths in the NUV region of 250–400, and 275 nm is the most suitable excitation wavelength for obtaining white light and manufacturing WLED devices from composite materials.

To further prove the energy transfer between NaGdF$_4$:Tb^{3+}/Eu^{3+} and C:N/Eu^{3+}, the luminescence attenuation curves of NaGdF$_4$:15%Tb^{3+}/1.5%Eu^{3+} and NGFTE-2.5@CNE were measured. As shown in Fig. 5(k), under excitation at 275 nm, the fluorescence lifetimes of NaGdF$_4$:15%Tb^{3+}/1.5%Eu^{3+} and NGFTE-2.5@CNE at 619 nm are 1,366.23 and 627.48 ns, respectively. This indicates that there is an energy transfer from NaGdF$_4$:Tb^{3+}/Eu^{3+} to C:N/Eu^{3+}. In summary, there are several energy transfer processes: (1) For NaGdF$_4$:Tb^{3+}/Eu^{3+}@C:N/Eu^{3+}, there are energy transfers between C:N/Eu^{3+} and the Ln^{3+} ions in NaGdF$_4$:Tb^{3+}/Eu^{3+}; (2) there is no Eu^{3+} excitation peak in the excitation spectra of Tb^{3+}, and there is Tb^{3+} excitation peak in the excitation spectra of Eu^{3+}, which indicates that there is an energy transfer from Tb^{3+} to Eu^{3+}; (3) there is a Gd^{3+} excitation peak in the excitation spectra of Tb^{3+}/Eu^{3+}, so there is an energy transfer from Gd^{3+} to Tb^{3+}/Eu^{3+}. The possible energy transfer mechanism is illustrated in the simplified energy level diagrams, as shown in Fig. S18 in the ESM. Of course, for complex material systems doped with multiple RE ions, the energy transfer process is also very complicated, and further research is needed in the future. Figure 5(l) shows the luminescence photos of samples in the liquid under NUV light irradiation. It can be seen from the photos that we obtained the blue, green, yellow, red, and white emissions independently.

2.5 Luminescence stability

We also conducted luminescence stability analysis, because the optical stability of the material is of considerable significance for practical applications. We studied the temperature-related optical properties of NaGdF$_4$:15%Tb^{3+}/1.5%Eu^{3+}@C:3N/5Eu^{3+}. Figure 6(a) shows the luminescence emission spectra of the NGFTE-2.5@CNE nanocomposites at different temperatures. Figure 6(b) shows the temperature-dependent function corresponding to the integrated intensity of the blue, green, and red emission intensities of NGFTE-2.5@CNE. As the temperature increases, the intensities of the blue, green, and red emission peaks decrease slightly. The results show that the NGFTE-2.5@CNE composite has good luminescence thermal stability. The calculated J-O parameters and the integrated emission peak area ratios of $^5D_0$-$^7F_2$/$^5D_0$-$^7F_1$ from the emission spectra in Fig. 6(a) are shown in Table S13 in the ESM. The values of Ω_2 are almost unchanged with temperature.

For LED devices, the luminescence stability of the sample under NUV light irradiation is the basis for exploring its practical application. Therefore, we have also explored the luminescence stability of CQDs:3N/5Eu^{3+}, NaGdF$_4$:15%Tb^{3+}/1.5%Eu^{3+}, and NGFTE-7.5@CNE under NUV light irradiation, as shown in Figs. 6(c)–6(g). The results show that the samples have good stability under NUV radiation and great application potential in WLEDs. The calculated J-O parameters and the integrated emission peak area ratios of $^5D_0$-$^7F_2$/$^5D_0$-$^7F_1$ from the emission spectra in Figs. 6(e) and 6(g) are shown in Tables S14 and S15 in the ESM. The values of Ω_2 are almost unchanged, indicating that the samples have good luminescence stability under NUV light irradiation.

2.6 Applications in WLEDs

We can not only construct WLEDs with CQDs:N/Eu^{3+}, NaGdF$_4$:Tb^{3+}, and NaGdF$_4$:Eu^{3+}, but also directly construct WLEDs with NaGdF$_4$:Tb^{3+}/Eu^{3+}@C:N/Eu^{3+} single composite material. To predict the application possibilities of the composite WLEDs, we took blue (CQDs:N/Eu^{3+}) emission as the calculation standard, and controlled the emission ratio of green (NaGdF$_4$:Tb^{3+}) and red (NaGdF$_4$:Eu^{3+}) luminescent materials to manufacture WLEDs. The white light emission with CRI greater than 90 and adjustable CCT, circadian action factor (CAF) and luminous efficacy of radiation (LER) was obtained. The schematic diagram of the WLED devices and the spectra used for optimization are shown in Figs. 7(a) and 7(b), respectively. Figures 7(c)–7(h) and Table S16 in the ESM summarize and present the optical properties obtained by extensive calculations and optimizations. As shown in Fig. 7(c), the CCT value increases as the ratio of CQDs:N/Eu^{3+} to NaGdF$_4$:Tb^{3+} and NaGdF$_4$:Eu^{3+} emission intensity increases. Therefore, to obtain white light with a lower color temperature, more green and red light emission should be used while reducing blue light emission. CAF stands for the impact of white light on human health. As shown in Fig. 7(d), the CAF increases as the ratio of CQDs:N/Eu^{3+} to NaGdF$_4$:Tb^{3+} and NaGdF$_4$:Eu^{3+} emission intensity increases. LER is a parameter that reflects visual performance. The higher the LER, the better the visual performance. As shown in Fig. 7(e), the LER nearly linearly depends on the ratio of CQDs:N/Eu^{3+} to NaGdF$_4$:Tb^{3+} and NaGdF$_4$:Eu^{3+} emission, and the LER decreases as the ratio

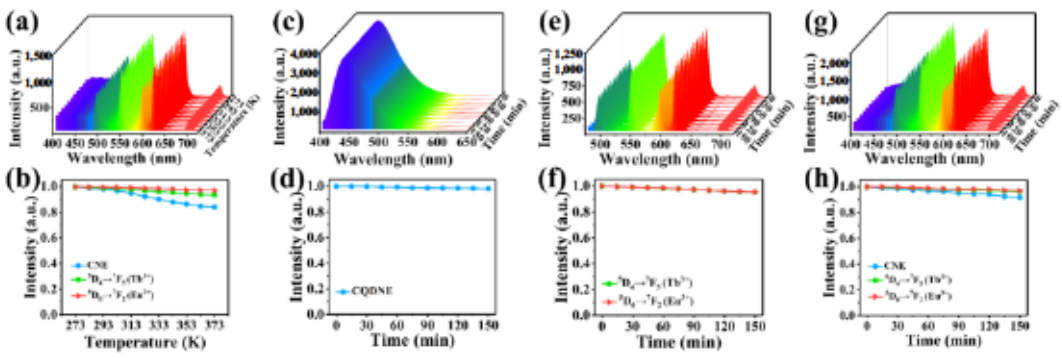

Figure 6 Luminescence stability of samples. (a) and (b) Temperature-dependent emission spectra and the corresponding fluorescence intensity changes of NGFTE-2.5@CNE. Luminescence stability under NUV light and the dependence of integrated area of emission peak on NUV irradiation time of ((c) and (d)) CQDs:3N/5Eu^{3+} (CQDNE), ((e) and (f)) NaGdF$_4$:15%Tb^{3+}/1.5%Eu^{3+}, and ((g) and (h)) NGFTE-7.5@CNE.

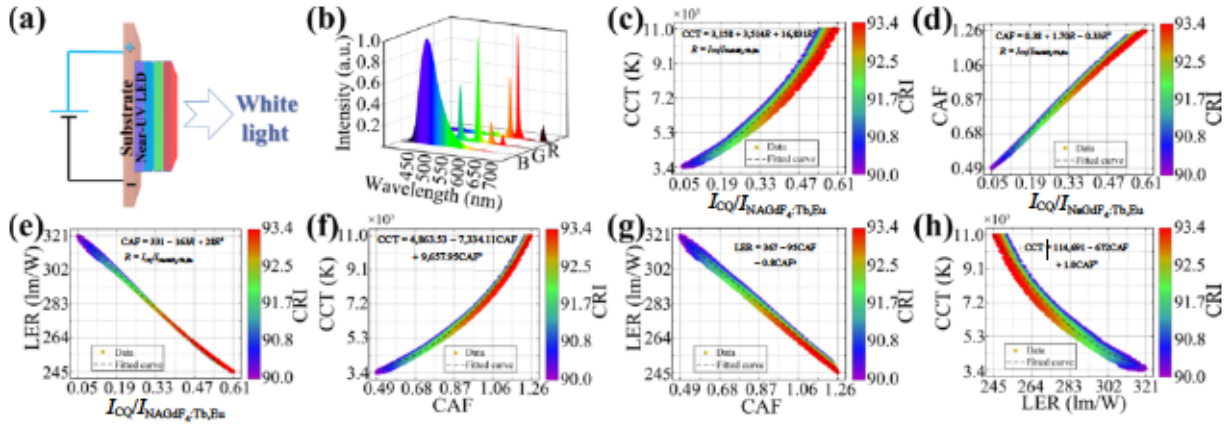

Figure 7 The calculated performance of WLEDs constructed with CQDs:N/Eu^{3+}, $NaGdF_4$:Tb^{3+}, and $NaGdF_4$:Eu^{3+}. (a) The schematic illustration of WLEDs. (b) The optimized emission spectra of the CQDs:N/Eu^{3+}, $NaGdF_4$:Tb^{3+}, and $NaGdF_4$:Eu^{3+}. The CCT (c), CAF (d), and LER (e) change with the emission ratio of CQD:N/Eu^{3+} to $NaGdF_4$:Tb^{3+} and $NaGdF_4$:Eu^{3+}. The CCT (f) and LER (g) as a function of CAF. (h) CCT as a function of LER. The color bar indicates the CRI with corresponding CCT.

increases. In addition, we also discussed the functional relationship between CCT, CAF and LER, as shown in Figs. 7(f)–7(h). It can be seen that the relationship between CCT, CAF and LER is almost linear. CCT increases with the increase of CAF. LER decreases with the increase of CAF. CCT also decreases with the increase of LER. The calculation results show that the obtained white light emission has the advantages of excellent color quality, great visual performance, and adjustable color temperature, which also provides theoretical support for subsequent research.

We also fabricated WLED devices with adjustable color temperature by depositing $NaGdF_4$:Tb^{3+}/Eu^{3+}@C:N/Eu^{3+} composite materials on 275 nm NUV-LED chips. As discussed above, changing the composite ratio of $NaGdF_4$:Tb^{3+}/Eu^{3+} and C:N/Eu^{3+} is the most direct way to change the R/G/B emission ratio of the sample, which is also a feasible scheme for obtaining full-color (R/G/B/W) emission. In this way, the spectra obtained by using the composite samples to the NUV-LED chips have the characteristic emission of these samples. In addition to changing the CCT of the WLED by using samples with different composite ratios, changing the voltage applied to the device is also an effective way to change the CCT of the WLED, which will be discussed in detail later. By the above two methods, we used samples with different composite ratios and changed the voltages to obtain WLED devices with cool white light (LED-1), neutral white light (LED-2, LED-3, LED-4, and LED-5), and warm white light (LED-6). The corresponding emission spectra, synthesis information, and related CIE chromaticity coordinates of the materials used in LED-4 and LED-6 are shown in Fig. S19 in the ESM. The spectra of the WLEDs are shown in Fig. 8(a). The CIE chromaticity coordinates of the WLEDs are located on the white light locus (Fig. 8(b)). Table S17 in the ESM summarizes the detailed performance of WLEDs composed of different samples. As expected, the CRI of WLEDs is between 91 and 95 and produces different CCTs in the range of 3,568–6,562 K, with excellent color quality and suitable CCT. The obtained LED-2 has a (0.337.0.339) CIE chromaticity coordinate (close to the standard white point); the CRI is up to 93, and the CCT is 5319 K. In addition, the CRI of LED-3 is up to 95, and LED-6 has an extremely small D_{uv} of 0.0006 and a maximum LER of 322 lm/W, which shows that the performance of WLEDs is excellent. The calculated J-O parameters and the emission peak area ratios of $^5D_0$-$^7F_2$/$^5D_0$-$^7F_1$ from the emission spectra in Fig. 8(a) are shown in Table S18 in the ESM. The values of Ω_2 are different for different WLED devices.

In order to further study the stability of the obtained WLED devices, the time-dependent luminescence of the WLED devices was tested (Fig. 8(c)). The light intensity decay rate of the obtained WLED devices is slow (Fig. 8(d)), which proves that the WLED devices have good stability. The calculated J-O parameters and the emission peak area ratios of $^5D_0$-$^7F_2$/$^5D_0$-$^7F_1$ from the emission spectra in Fig. 8(c) are shown in Table S19 in the ESM. The values of Ω_2 change slightly with time.

We also explored the effect of applied voltage on WLED light emission by changing the voltage applied to the devices, as shown in Fig. 9(a). As the applied voltage increases, the luminescence intensity of the sample will increase, gradually changing from cold white light to neutral white light. When the voltage is low, the emission mainly comes from C:3N/5Eu^{3+}, which indicates that C:3N/5Eu^{3+} is easier to excite at a relatively low voltage. Then, as the applied voltage increases, the emission of $NaGdF_4$:15%Tb^{3+}/1.5%Eu^{3+} will be clearer. This indicates that higher applied voltage is required to obtain white light with a lower color temperature. The calculated J-O parameters and the emission peak area ratios of $^5D_0$-$^7F_2$/$^5D_0$-$^7F_1$ from the emission spectra in Fig. 9(a) are shown in Table S20 in the ESM. The values of Ω_2 increase slightly with the voltages. In summary, the WLED devices with a wide CCT range that we have obtained show great potential in WLED applications by $NaGdF_4$:Tb^{3+}/Eu^{3+}@C:N/Eu^{3+} single phosphors due to their excellent color quality and visual performance.

In addition to WLEDs, we also produced green, yellow-green,

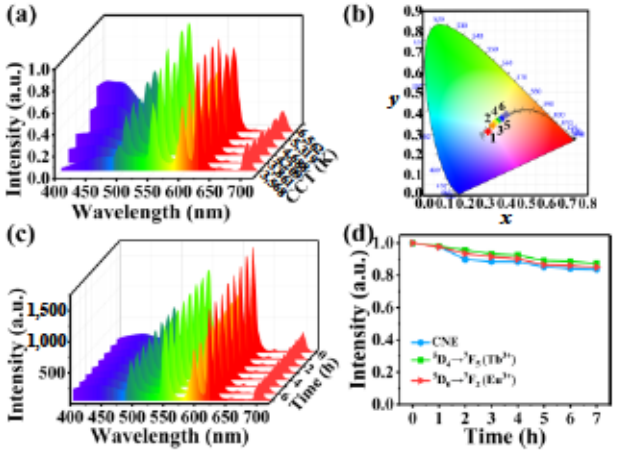

Figure 8 Performance of WLEDs constructed with white emitting $NaGdF_4$:Tb^{3+}/Eu^{3+}@C:N/Eu^{3+} single phosphors. (a) and (b) Luminescence spectra of LEDs and their CIE chromaticity diagram of WLEDs with different CCTs. (c) and (d) The time-dependent luminescence and the integrated emission intensity of LED-3 (6.2 V) as a function of time.

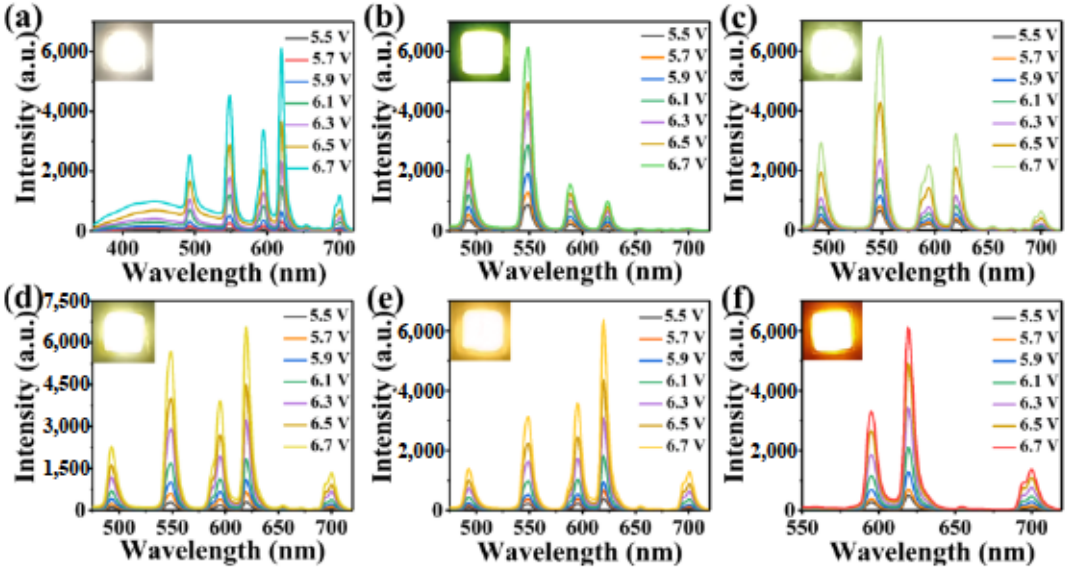

Figure 9 Emission spectra of white and multicolor LED devices at different voltages: (a) white (NGFTE-7.5@CNE), (b) green ($NaGdF_4$:15%Tb^{3+}), (c) yellow-green ($NaGdF_4$:15%Tb^{3+}/1%Eu^{3+}), (d) yellow ($NaGdF_4$:15%Tb^{3+}/1.5%Eu^{3+}), (e) orange-red ($NaGdF_4$:15%Tb^{3+}/1.75%Eu^{3+}), and (f) red ($NaGdF_4$:15%Eu^{3+}) phosphor-based LEDs, respectively. The illustrations are the corresponding photographs with a voltage of 6.5 V.

yellow, orange-red, and red LEDs. The color of the LEDs devices can be adjusted by adjusting the concentration ratio of Tb^{3+}/Eu^{3+}. The obtained multi-color light-emitting diode has good performance. The related variable voltage emission spectra and photos are shown in Figs. 9(b)–9(f). Similar to the WLED devices, the emission intensity of the WLED gradually increases as the applied voltage increases. The calculated J-O parameters and the emission peak area ratios of $^5D_0$-$^7F_2$/$^5D_0$-$^7F_1$ from the emission spectra in Figs. 9(c)–9(f) are shown in Tables S21–S24 in the ESM. The values of Ω_2 increase slightly with the voltages.

3 Conclusions

Combining monochromatic fluorescent materials to obtain single-phase white light composite materials with excellent performance is an important part of promoting the development of WLED applications. In summary, the DFT was employed to optimize the structures of the C:N/Eu^{3+} and $NaGdF_4$:Tb^{3+}/Eu^{3+}, and calculate the work function, optical properties, and charge differential density. The results of DFT calculation and experimental characterization show that C atoms cannot be replaced by Eu^{3+}, but C atoms are more favorable for anchoring Eu^{3+} single atoms. And the heterojunction of the C:N/Eu^{3+} and $NaGdF_4$:Tb^{3+}/Eu^{3+} was successfully constructed, which proved the superiority of this new type of composite material. The $NaGdF_4$:Tb^{3+}/Eu^{3+}@C:N/Eu^{3+} composite material was successfully synthesized by solvothermal method and hydrothermal method. To further research on the luminescence properties, it is confirmed that the composite material combines the structure and luminescence characteristics of C:N/Eu^{3+} and $NaGdF_4$:Tb^{3+}/Eu^{3+}. The HRTEM images proved that the CQDs formed a carbon layer on the surface of $NaGdF_4$ particles. Through the HAADF-STEM images shooting of the composite material, it is found that the Eu^{3+} single atom structure is formed in the surface carbon layer, which also confirms that the nitrogen-containing carbon material is beneficial to anchoring the RE single atoms. The experimental results show that N/Eu^{3+} can enhance the luminous intensity of CQDs. We believe that building a RE single-atom structure may be a new strategy to improve the luminescence of nitrogen-containing carbon materials. Finally, by tuning the co-doping concentration of Tb^{3+} and Eu^{3+} in $NaGdF_4$ and the mixing ratio of C:N/Eu^{3+}, the emissivity of red, green, and blue was successfully adjusted to make the $NaGdF_4$:Tb^{3+}/Eu^{3+}@C:N/Eu^{3+} composite material have excellent color quality and white light. This new functional RE luminescent material has successfully realized the WLED devices with excellent color performance (CRI is up to 95) and controllable CCT (3,568–6,562 K). It is confirmed that they have great potential in WLED applications.

Acknowledgements

This work was supported by the National Natural Science Foundation of China (Nos. 21871079 and 11774128), the Natural Science Foundation of Shandong Province (Nos. ZR2018JL003 and 2019KJJ003), and the National Science Foundation (No. 1945558).

Electronic Supplementary Material: Supplementary material (experimental section, detailed characterization, spectral optimization, and computational details) is available in the online version of this article at https://doi.org/10.1007/s12274-021-3886-x.

References

[1] Nair, G. B.; Swart, H. C.; Dhoble, S. J. A review on the advancements in phosphor-converted light emitting diodes (pc-LEDs): Phosphor synthesis, device fabrication and characterization. *Prog. Mater. Sci.* **2020**, *109*, 100622.

[2] Joo, W. J.; Kyoung, J.; Esfandyarpour, M.; Lee, S. H.; Koo, H.; Song, S.; Kwon, Y. N.; Song, S. H.; Bae, J. C.; Jo, A. et al. Metasurface-driven OLED displays beyond 10, 000 pixels per inch. *Science* **2020**, *370*, 459–463.

[3] Bando, Y. A new path in lighting and display: White light emitting diode with a single active layer. *Sci. Bull.* **2021**, *66*, 860–861.

[4] Chen, Z.; Ho, C. L.; Wang, L. Q.; Wong, W. Y. Single-molecular white-light emitters and their potential WOLED applications. *Adv. Mater.* **2020**, *32*, 1903269.

[5] Ding, D. X.; Wang, Z. C.; Li, C. Y.; Zhang, J.; Duan, C. B.; Wei, Y.; Xu, H. Highly efficient and color-stable thermally activated delayed fluorescence white light-emitting diodes featured with single-doped single emissive layers. *Adv. Mater.* **2020**, *32*, 1906950.

[6] Li, D. B.; Jiang, K.; Sun, X. J.; Guo, C. L. AlGaN photonics: Recent advances in materials and ultraviolet devices. *Adv. Opt. Photonics* **2018**, *10*, 43–110.

[7] Wang, L.; Wang, X.; Bertram, F.; Sheng, B. W.; Hao, Z. B.; Luo, Y.; Sun, C. Z.; Xiong, B.; Han, Y. J.; Wang, J. et al. Color-tunable 3D

InGaN/GaN multi-quantum-well light-emitting-diode based on microfacet emission and programmable driving power supply. *Adv. Opt. Mater.* **2021**, *9*, 2001400.

[8] Dang, P. P.; Li, G. G.; Yun, X. H.; Zhang, Q. Q.; Liu, D. J.; Lian, H. Z.; Shang, M. M.; Lin, J. Thermally stable and highly efficient red-emitting Eu^{3+}-doped $Cs_3GdGe_3O_9$ phosphors for WLEDs: Non-concentration quenching and negative thermal expansion. *Light:Sci. Appl.* **2021**, *10*, 29.

[9] Huang, X. Y.; Wang, S. Y.; Li, B.; Sun, Q.; Guo, H. High-brightness and high-color purity red-emitting $Ca_3Lu(AlO)_3(BO_3)_4$: Eu^{3+} phosphors with internal quantum efficiency close to unity for near-ultraviolet-based white-light-emitting diodes. *Opt. Lett.* **2018**, *43*, 1307–1310.

[10] Wei, Y.; Yang, H.; Gao, Z. Y.; Liu, Y. X.; Xing, G. C.; Dang, P. P.; Al Kheraif, A. A.; Li, G. G.; Lin, J.; Liu, R. S. Strategies for designing antithermal-quenching red phosphors. *Adv. Sci.* **2020**, *7*, 1903060.

[11] Mondal, N.; De, A.; Samanta, A. Achieving near-unity photoluminescence efficiency for blue-violet-emitting perovskite nanocrystals. *ACS Energy Lett.* **2019**, *4*, 32–39.

[12] Luo, J. J.; Wang, X. M.; Li, S. R.; Liu, J.; Guo, Y. M.; Niu, G. D.; Yao, L.; Fu, Y. H.; Gao, L.; Dong, Q. S. et al. Efficient and stable emission of warm-white light from lead-free halide double perovskites. *Nature* **2018**, *563*, 541–545.

[13] Hoerder, G. J.; Seibald, M.; Baumann, D.; Schröder, T.; Peschke, S.; Schmid, P. C.; Tyborski, T.; Pust, P.; Stoll, I.; Bergler, M. et al. $Sr[Li_2Al_2O_2N_2]$: Eu^{2+}-A high performance red phosphor to brighten the future. *Nat. Commun.* **2019**, *10*, 1824.

[14] Wang, Z. F.; Yuan, F. L.; Li, X. H.; Li, Y. C.; Zhong, H. Z.; Fan, L. Z.; Yang, S. H. 53% efficient red emissive carbon quantum dots for high color rendering and stable warm white-light-emitting diodes. *Adv. Mater.* **2017**, *29*, 1702910.

[15] Zhao, M.; Xia, Z. G.; Huang, X. X.; Ning, L. X.; Gautier, R.; Molokeev, M. S.; Zhou, Y. Y.; Chuang, Y. C.; Zhang, Q. Y.; Liu, Q. L. et al. Li substituent tuning of LED phosphors with enhanced efficiency, tunable photoluminescence, and improved thermal stability. *Sci. Adv.* **2019**, *5*, eaav0363.

[16] Yang, Z. W.; Gao, M. Y.; Wu, W. J.; Yang, X. Y.; Sun, X. W.; Zhang, J. H.; Wang, H. C.; Liu, R. S.; Han, C. Y.; Yang, H. et al. Recent advances in quantum dot-based light-emitting devices: Challenges and possible solutions. *Mater. Today* **2019**, *24*, 69–93.

[17] Zhou, G. J.; Su, B. B.; Huang, J. L.; Zhang, Q. Y.; Xia, Z. G. Broad-band emission in metal halide perovskites: Mechanism, materials, and applications. *Mater. Sci. Eng. R: Rep.* **2020**, *141*, 100548.

[18] Wang, Z. F.; Liu, Y.; Zhen, S. J.; Li, X. X.; Zhang, W. G.; Sun, X.; Xu, B. Y.; Wang, X.; Gao, Z. H.; Meng, X. G. Gram-scale synthesis of 41% efficient single-component white-light-emissive carbonized polymer dots with hybrid fluorescence/phosphorescence for white light-emitting diodes. *Adv. Sci.* **2020**, *7*, 1902688.

[19] Boddula, R.; Tagare, J.; Singh, K.; Vaidyanathan, S. White light-emissive europium complexes and their versatile applications. *Mater. Chem. Front.* **2021**, *5*, 3159–3175.

[20] Yuan, H. L.; Massuyeau, F.; Gautier, N.; Kama, A. B.; Faulques, E.; Chen, F.; Shen, Q.; Zhang, L. M.; Paris, M.; Gautier, R. Doped lead halide white phosphors for very high efficiency and ultra-high color rendering. *Angew. Chem., Int. Ed.* **2020**, *59*, 2802–2807.

[21] Xu, H. Y.; Yu, W. J.; Pan, K.; Wang, G. F.; Zhu, P. F. Confinement and antenna effect for ultrasmall Y_2O_3: Eu^{3+} nanocrystals supported by MOF with enhanced near-UV light absorption thereby enhanced luminescence and excellently multifunctional applications. *Nano Res.* **2021**, *14*, 720–729.

[22] Gao, G. Y.; Li, Y. N.; Yu, W. J.; Wang, G. F.; Zhu, P. F.; Qin, W. P.; Wang, D. S. Enhanced luminescence through interface energy transfer in hierarchical heterogeneous nanocomposites and application in white LEDs. *J. Colloid Interface Sci.* **2021**, *583*, 204–213.

[23] Xu, L. N.; Li, Y. N.; Pan, Q. J.; Wang, D.; Li, S. J.; Wang, G. F.; Chen, Y. J.; Zhu, P. F.; Qin, W. P. Dual-mode light-emitting lanthanide metal-organic frameworks with high water and thermal stability and their application in white LEDs. *ACS Appl. Mater. Interfaces* **2020**, *12*, 18934–18943.

[24] Zhang, W. Y.; Thapa, S.; Sun, Y.; Norville, S.; Zhu, H. Y.; Zhu, P. F.; Wang, G. F.; Qin, W. P. Substitution of Pb with Mn^{2+}/Nd^{3+} to improve the luminescence and thermal stability of Cs_4PbBr_6. *Chem. Eng. J.* **2021**, *423*, 130186.

[25] Wang, L.; Li, W. T.; Yin, L. Q.; Liu, Y. J.; Guo, H. Z.; Lai, J. W.; Han, Y.; Li, G.; Li, M.; Zhang, J. H. et al. Full-color fluorescent carbon quantum dots. *Sci. Adv.* **2020**, *6*, eabb6772.

[26] Rad, R. R.; Gualdrón-Reyes, A. F.; Masi, S.; Ganji, B. A.; Taghavinia, N.; Gené-Marimon, S.; Palomares, E.; Mora-Seró, I. Tunable carbon-$CsPbI_3$ quantum dots for white LEDs. *Adv. Opt. Mater.* **2021**, *9*, 2001508.

[27] Qin, X.; Liu, X. W.; Huang, W.; Bettinelli, M.; Liu, X. G. Lanthanide-activated phosphors based on 4f-5d optical transitions: Theoretical and experimental aspects. *Chem. Rev.* **2017**, *117*, 4488–4527.

[28] Wang, G. F.; Peng, Q.; Li, Y. D. Lanthanide-doped nanocrystals: Synthesis, optical-magnetic properties, and applications. *Acc. Chem. Res.* **2011**, *44*, 322–332.

[29] Hong, F.; Xu, H. P.; Pang, G.; Liu, G. X.; Dong, X. T.; Yu, W. S. Moisture resistance, luminescence enhancement, energy transfer and tunable color of novel core-shell structure $BaGeF_6$:Mn^{4+} phosphor. *Chem. Eng. J.* **2020**, *390*, 124579.

[30] Ding, M. Y.; Dong, B.; Lu, Y.; Yang, X. F.; Yuan, Y. J.; Bai, W. F.; Wu, S. T.; Ji, Z. G.; Lu, C. H.; Zhang, K. et al. Energy manipulation in lanthanide-doped core-shell nanoparticles for tunable dual-mode luminescence toward advanced anti-counterfeiting. *Adv. Mater.* **2020**, *32*, 2002121.

[31] Zhang, N. Q.; Ye, C. L.; Yan, H.; Li, L. C.; He, H.; Wang, D. S.; Li, Y. D. Single-atom site catalysts for environmental catalysis. *Nano Res.* **2020**, *13*, 3165–3182.

[32] Li, X. Y.; Rong, H. P.; Zhang, J. T.; Wang, D. S.; Li, Y. D. Modulating the local coordination environment of single-atom catalysts for enhanced catalytic performance. *Nano Res.* **2020**, *13*, 1842–1855.

[33] Yang, J. R.; Li, W. H.; Wang, D. S.; Li, Y. D. Single-atom materials: Small structures determine macroproperties. *Small Struct.* **2021**, *2*, 2000051.

[34] Zhuang, Z. C.; Kang, Q.; Wang, D. S.; Li, Y. D. Single-atom catalysis enables long-life, high-energy lithium-sulfur batteries. *Nano Res.* **2020**, *13*, 1856–1866.

[35] Wang, Y.; Mao, J.; Meng, X. G.; Yu, L.; Deng, D. H.; Bao, X. H. Catalysis with two-dimensional materials confining single atoms: Concept, design, and applications. *Chem. Rev.* **2019**, *119*, 1806–1854.

[36] Wang, Y.; Zheng, X. B.; Wang, D. S. Design concept for electrocatalysts. *Nano Res.* **2021**, in press, http://doi.org/10.1007/s12274-021-3794-0.

[37] Ji, S. F.; Qu, Y.; Wang, T.; Chen, Y. J.; Wang, G. F.; Li, X.; Dong, J. C.; Chen, Q. Y.; Zhang, W. Y.; Zhang, Z. D. et al. Rare-earth single erbium atoms for enhanced photocatalytic CO_2 reduction. *Angew. Chem., Int. Ed.* **2020**, *59*, 10651–10657.

[38] Liu, J. Y.; Kong, X.; Zheng, L. R.; Guo, X.; Liu, X. F.; Shui, J. L. Rare earth single-atom catalysts for nitrogen and carbon dioxide reduction. *ACS Nano* **2020**, *14*, 1093–1101.

[39] Gao, C.; Low, J. X.; Long, R.; Kong, T. T.; Zhu, J. F.; Xiong, Y. J. Heterogeneous single-atom photocatalysts: Fundamentals and applications. *Chem. Rev.* **2020**, *120*, 12175–12216.

[40] Gao, G. P.; Jiao, Y.; Waclawik, E. R.; Du, A. J. Single atom (Pd/Pt) supported on graphitic carbon nitride as an efficient photocatalyst for visible-light reduction of carbon dioxide. *J. Am. Chem. Soc.* **2016**, *138*, 6292–6297.

[41] Xiong, Y.; Sun, W. M.; Han, Y. H.; Xin, P. Y.; Zheng, X. S.; Yan, W. S.; Dong, J. C.; Zhang, J.; Wang, D. S.; Li, Y. D. Cobalt single atom site catalysts with ultrahigh metal loading for enhanced aerobic oxidation of ethylbenzene. *Nano Res.* **2021**, *14*, 2418–2423.

[42] Xu, Q.; Guo, C. X.; Tian, S. B.; Zhang, J.; Chen, W. X.; Cheong, W. C.; Gu, L.; Zheng, L. R.; Xiao, J. P.; Liu, Q. et al. Coordination structure dominated performance of single-atomic Pt catalyst for anti-Markovnikov hydroboration of alkenes. *Sci. China Mater.* **2020**, *63*, 972–981.

[43] Han, A. J.; Wang, B. Q.; Kumar, A.; Qin, Y. J.; Jin, J.; Wang, X. H.;

Yang, C.; Dong, B.; Jia, Y.; Liu, J. F. et al. Recent advances for MOF-derived carbon-supported single-atom catalysts. *Small Methods* **2019**, *3*, 1800471.

[44] Wang, D.; Zhao, C.; Gao, G. Y.; Xu, L. N.; Wang, G. F.; Zhu, P. F. Multifunctional $NaLnF_4$@MOF-Ln nanocomposites with dual-mode luminescence for drug delivery and cell imaging. *Nanomaterials* **2019**, *9*, 1274.

[45] Song, Y.; Shao, B. Q.; Feng, Y.; Lü, W.; Liu, G. X.; You, H. P. A novel strategy to enhance the luminescence performance of $NaGdF_4$: Ln^{3+} nanocrystals. *Dalton Trans.* **2016**, *45*, 9468–9476.

[46] Bouzas-Ramos, D.; Canga, J. C.; Mayo, J. C.; Sainz, R. M.; Encinar, J. R.; Costa-Fernandez, J. M. Carbon quantum dots codoped with nitrogen and lanthanides for multimodal imaging. *Adv. Funct. Mater.* **2019**, *29*, 1903884.